chemosensors

MDPI

Article

$CoNiTe_2$ Nanomaterials as an Efficient Non-Enzymatic Electrochemical Sensing Platform for Detecting Dopamine

Zhi-Yuan Wang [1], Chi-Hung Shen [1], Shih-Hao Yang [1], Han-Wei Chang [2,3,*] and Yu-Chen Tsai [1,*]

[1] Department of Chemical Engineering, National Chung Hsing University, Taichung 40227, Taiwan; dog987784@gmail.com (Z.-Y.W.); glun25@gmail.com (C.-H.S.); g112065059@mail.nchu.edu.tw (S.-H.Y.)
[2] Department of Chemical Engineering, National United University, Miaoli 360302, Taiwan
[3] Pesticide Analysis Center, National United University, Miaoli 360302, Taiwan
* Correspondence: hwchang@nuu.edu.tw (H.-W.C.); yctsai@dragon.nchu.edu.tw (Y.-C.T.); Tel.: +886-37-382216 (H.-W.C.); +886-4-22857257 (Y.-C.T.)

Abstract: Dopamine (DA) is an important catecholamine neurotransmitter in the mammalian central nervous system that affects many physiological functions. Hence, a highly sensitive and selective sensing platform is necessary for quantification of DA in the human body. In this study, ternary transition metal tellurides of $CoNiTe_2$ were successfully synthesized using the hydrothermal method. The proposed $CoNiTe_2$ nanomaterials were dispersed well in Nafion to form a well-dispersed suspension and, when dropped on a glassy carbon electrode (GCE) as the working electrode ($CoNiTe_2$/Nafion/GCE) for electrochemical non-enzymatic DA sensing, displayed excellent electrocatalytic activity for dopamine electrooxidation. The morphology and physical/chemical properties of $CoNiTe_2$ nanomaterials were characterized using field emission scanning electron microscopy (FESEM), transmission electron microscopy (TEM), X-ray diffraction (XRD), and X-ray photoelectron spectroscopy (XPS). In order to obtain the best electrochemical response to DA from the fabricated $CoNiTe_2$/Nafion/GCE, the experimental conditions of electrochemical sensing, including the $CoNiTe_2$ loading amounts and pH values of the phosphate buffer solution (PBS), were explored to achieve the best electrochemical sensing performance. Under optimal conditions (2 mg of $CoNiTe_2$ and pH 6.0 of PBS), the fabricated $CoNiTe_2$/Nafion/GCE showed excellent electrocatalytic activity of DA electrooxidation. The $CoNiTe_2$/Nafion/GCE sensing platform demonstrated excellent electrochemical performance owing to the optimal structural and electronic characteristics originating from the synergistic interactions of bimetallic Co and Ni, the low electronegativity of Te atoms, and the unique morphology of the $CoNiTe_2$ nanorod. It exhibited a wide linear range from 0.05 to 100 μM, a high sensitivity of 1.2880 μA μM^{-1} cm^{-2}, and a low limit of detection of 0.0380 μM, as well as acceptable selectivity for DA sensing. Therefore, the proposed $CoNiTe_2$/Nafion/GCE could be considered a promising electrode material for electrochemical non-enzymatic DA sensing.

Keywords: $CoNiTe_2$ transition metal tellurides; electrochemical non-enzymatic dopamine sensing; morphology

Citation: Wang, Z.-Y.; Shen, C.-H.; Yang, S.-H.; Chang, H.-W.; Tsai, Y.-C. $CoNiTe_2$ Nanomaterials as an Efficient Non-Enzymatic Electrochemical Sensing Platform for Detecting Dopamine. *Chemosensors* **2024**, *12*, 110. https://doi.org/10.3390/chemosensors12060110

Received: 17 May 2024
Revised: 7 June 2024
Accepted: 11 June 2024
Published: 13 June 2024

1. Introduction

Carlsson et al. (1958) reported that dopamine (DA) is a key neurotransmitter in the brain and is used as an immediate precursor in the biosynthesis of noradrenaline [1]. Current data reveal that DA is the predominant neurotransmitter expressed in the mammalian central nervous system (accounting for 80% of the catecholamine content in the brain) [2]. The amount of DA released correlates exclusively to diverse brain functions and is expressed specifically in the ventral tegmental area (VTA) of the midbrain, the substantia nigra pars compacta, and the hypothalamic arcuate nucleus of the human brain [3]. VTA dopaminergic activity controls natural motivation, reward prediction, and contextual learning [4,5]. Parkinson's disease (PD), one of the most common neurodegenerative

disorders, is linked to abnormal dopamine release in the substantia nigra pars compacta. PD is diagnosed by characteristic motor tremors [6,7]. The hypothalamic arcuate nucleus' dopaminergic neurons are essential in regulating prolactin release. Prolactin is a protein hormone synthesized and secreted by lactotropic cells in the anterior pituitary gland and is involved in the prolactin homeostasis of the body [8,9].

Unquestionably, finding a precise and efficient method to quickly detect DA level deviations, thereby mitigating the societal and economic burdens associated with neurological disorders, is urgent. So far, analytical methods such as fluorescence [10], colorimetry [11], chemiluminescence [12], high-performance liquid chromatography (HPLC) [13], capillary electrophoresis (CE) [14], and electrochemistry [15,16] have been used to detect DA. Electrochemical methods stand out among the conventional analytical techniques because they are affordable, have a short analysis time, give an immediate response, and are user-friendly [17,18]. Electrochemical analytical methods detect DA using two sensing platforms: enzymatic and non-enzymatic. Although enzymatic sensors demonstrate high sensitivity and specificity, they are expensive, are complex to produce, have limited reproducibility, and are susceptible to environmental factors such as pH and temperature [19]. An electrochemical non-enzymatic DA sensor needs to be developed to overcome these drawbacks.

Previous reports reveal that electrochemical DA sensors based on transition metal chalcogenides (including transition metal sulfides (TMSs) [20], transition metal selenides (TMSs) [21], and transition metal tellurides (TMTs) [22]) have been successfully used in the development of electrode materials. Transition metal chalcogenides are a promising choice for electrode materials because of their excellent conductivity, abundant active sites, simplified synthesis procedures, and low preparation costs [23]. Furthermore, the electronegativity of Te (2.1) is low compared to S (2.58) and Se (2.55), resulting in weaker bonds between transition metals and Te. This facilitates electrochemical redox reactions [24]. These characteristics make TMTs suitable for extensive applications in the electrochemical field such as in supercapacitors [25], water splitting [26], and CO_2 reduction [27]. From the above-mentioned reports, TMTs have attracted significant attention in the electrochemical field due to the synergic effect caused by multiple redox-active transition metals, the low electronegativity of Te, and their unique structural features. In TMTs, the electronegativity of Te is lower than S and Se, which would tend to weaken covalent bonding between the transition metal and Te. Electronic structure tuning in transition metal chalcogenides should facilitate ion insertion/extraction and electron transport to give an excellent electrochemical performance. Nevertheless, the existing literature provides limited information on TMTs' use as electrochemical biosensors, especially in DA sensing.

In this study, we prepared $CoNiTe_2$ ternary transition metal telluride nanomaterials using the hydrothermal method. We fabricated a $CoNiTe_2$/Nafion/glassy carbon electrode (GCE) sensing platform by drop-casting the prepared $CoNiTe_2$/Nafion nanocomposite on GCE. The $CoNiTe_2$/Nafion nanocomposite catalyzed DA electrochemical redox to deliver remarkable electrochemical performance through the synergistic effects of bimetallic Co and Ni, the relatively low electronegativity of Te, and the unique features of nanorod morphology.

2. Materials and Methods

2.1. Reagents

Cobalt (II) chloride hexahydrate ($CoCl_2 \cdot 6H_2O$), nickel (II) chloride hexahydrate ($NiCl_2 \cdot 6H_2O$), hydrazine monohydrate ($N_2H_4 \cdot H_2O$), and ethylenediamine were obtained from Alfa Aesar (Ward Hill, MA, USA). Tellurium powder (~200 mesh), Nafion solution (5 wt % in mixture of lower aliphatic alcohols and water), sodium phosphate dibasic (Na_2HPO_4), sodium phosphate monobasic (NaH_2PO_4), dopamine hydrochloride (DA), uric acid (UA), and L-ascorbic acid (AA) were purchased from Sigma-Aldrich (St. Louis, MO, USA). Anhydrous ethanol (C_2H_5OH, 99.9%) was purchased from J.T. Baker (Phillipsburg, NJ, USA). The deionized water (DI water) was produced using a Milli-Q water purification system from Millipore Co. (Bedford, MA, USA). All chemicals were analytical grade and were used as received without further purification.

2.2. Synthesis of $CoNiTe_2$ Nanomaterials

The $CoNiTe_2$ transition metal tellurides were successfully synthesized via a facile hydrothermal method. As is typical, 0.409 g $CoCl_2 \cdot 6H_2O$ and 0.411 g $NiCl_2 \cdot 6H_2O$ were precisely weighed and fully dissolved in 30 mL DI water by stirring for 30 min to form solution (A). At the same time, 0.235 g Te powder was dispersed into 8 mL ethylenediamine and stirred for 30 min to form solution (B). In the next step, solution (B) was added dropwise to solution (A) and stirred for 30 min to make sure all the reactants were totally dissolved. After that, 8 mL $N_2H_4 \cdot H_2O$ was selected as the reducing agent and added to the mixture. The mixture was allowed to stir until a black precipitate appeared. Subsequently, the obtained black precipitate containing the Ni–Co telluride precursor was transferred into a 100 mL Teflon-lined stainless autoclave and heated to 180 °C for 12 h in an oven. Under mild hydrothermal conditions, the as-fabricated Ni–Co telluride precursor went through the amorphous–crystalline phase transformation induced by incorporated metal ions. Finally, the resulting $CoNiTe_2$ nanomaterials were cleaned by with DI water and anhydrous ethanol in a centrifuge 3 times, and then dried in the oven overnight. Then, the dried $CoNiTe_2$ nanomaterials were collected for subsequent characterization. A schematic illustration of the synthesis of the $CoNiTe_2$ nanomaterials is shown in Figure 1.

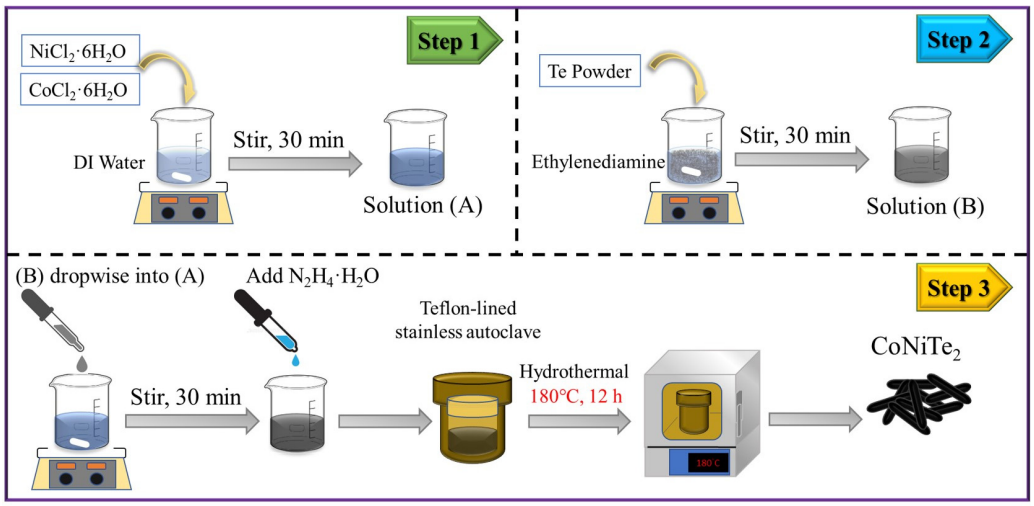

Figure 1. The schematic diagram for the synthesis of $CoNiTe_2$.

2.3. Fabrication of $CoNiTe_2$/Nafion/GCE Working Electrode

To prepare the glassy carbon electrode (GCE, diameter 3 mm, Tokai Carbon, Tokyo, Japan) for use, a thorough polishing procedure was performed by using 0.3 μm and 0.05 μm alumina slurries. Subsequently, the electrode was subjected to a rapid ultrasonic cleaning process using deionized (DI) water and anhydrous ethanol, followed by drying in a 70 °C oven. Next, 2 mg $CoNiTe_2$ nanomaterials were weighed and dispersed in 1 mL 0.5 wt % Nafion solution through ultrasonication for 30 min to form a well-distributed suspension. To fabricate the working electrode, 6 μL of the suspension was dropped on the precleaned GCE (bare GCE) and dried in the oven at 60 °C for 20 min. In this way, $CoNiTe_2$/Nafion/GCE was obtained for the following electrochemical measurements.

2.4. Characterizations

The morphology was characterized using field emission scanning electron microscopy (FESEM, JSM-7800F, JEOL, Akishima, Japan) and transmission electron microscopy (TEM, JEM-2100F, JEOL, Akishima, Japan). The crystal phase was analyzed by using X-ray diffraction (XRD) (D8 Discover X-ray diffractometer with Cu Kα radiation (Bruker, Karlsruhe, Germany). The chemical structure and composition were determined by using X-ray photoelectron spectroscopy (XPS, PHI-5000 Versaprobe, ULVAC-PHI, Chigasaki, Japan). Electrochemical measurements were performed by using an electrochemical analyzer (Au-

tolab, model PGSTAT 30, Eco Chemie, Utrecht, The Netherlands) in a three-electrode system (the as-prepared samples modified with GCE were used as the working electrode, along with a platinum wire counter electrode and an Ag/AgCl (3 M KCl) reference electrode). All electrochemical measurements were conducted in 0.1 M phosphate-buffered saline (PBS) as the supporting electrolyte in the absence or presence of DA. Cyclic voltammetry (CV) and differential pulse voltammetry (DPV) measurements were taken in the working potential window of −0.2~1.0 V and 0~0.5 V. The DPV operational parameters (in 0.1 M PBS at pH 6.0) were optimized as follows: modulation time of 0.050 s, modulation amplitude of 0.050 V, pulse width of 0.050 s, internal time of 0.200 s, and step potential of 0.004 V.

3. Results and Discussion

The FESEM image (Figure 2a) revealed that the $CoNiTe_2$ surface is composed of a rod-like structure (approximately 700 nm in length) with numerous short nanorods (approximately several nanometers in length) growing on it. The short nanorods provide abundant electrochemical active sites and this boosts electronic/ionic transport during the subsequent electrochemical measurements. The TEM image (Figure 2b) revealed that the $CoNiTe_2$ nanomaterial's inner structure concurred with the surface morphology observed by FESEM. Figure 3a–d show the scanning TEM (STEM) images and their corresponding EDS mapping for $CoNiTe_2$. These affirm that the $CoNiTe_2$ nanorod structure comprises well-distributed Co, Ni, and Te elements. The EDS spectrum (Figure 3e) of the $CoNiTe_2$ nanomaterials further revealed that the atomic ratio of Co, Ni, and Te is approximately 0.2:0.2:0.5, which is close to the theoretical atomic ratio of $CoNiTe_2$. The $CoNiTe_2$ nanomaterials were then characterized by X-ray diffraction. The standard XRD pattern of $CoNiTe_2$ (JCPDS No. 65-8961) [28] was obtained.

The XRD pattern identified the structure and phase composition of the $CoNiTe_2$ nanomaterials based on the standard patterns in the crystalline phase of $CoNiTe_2$ (JCPDS No. 65-8961) [28], as shown in Figure 4. In the XRD pattern of the $CoNiTe_2$ nanomaterials, the diffraction peaks located at 2θ equaling 31.1°, 43.2°, 45.9°, 56.5°, and 58.9° are attributed to the (101), (102), (110), (201), and (103) planes, respectively (indexed to the crystalline phase of $CoNiTe_2$). These characterizations confirm that the $CoNiTe_2$ ternary transition metal tellurides were successfully synthesized via a facile hydrothermal method.

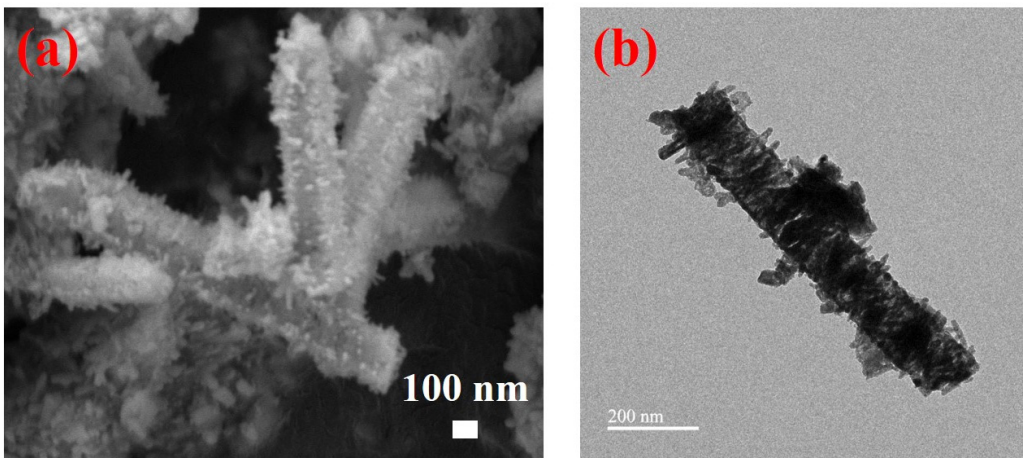

Figure 2. (**a**) FESEM image and (**b**) TEM image of $CoNiTe_2$ nanomaterials.

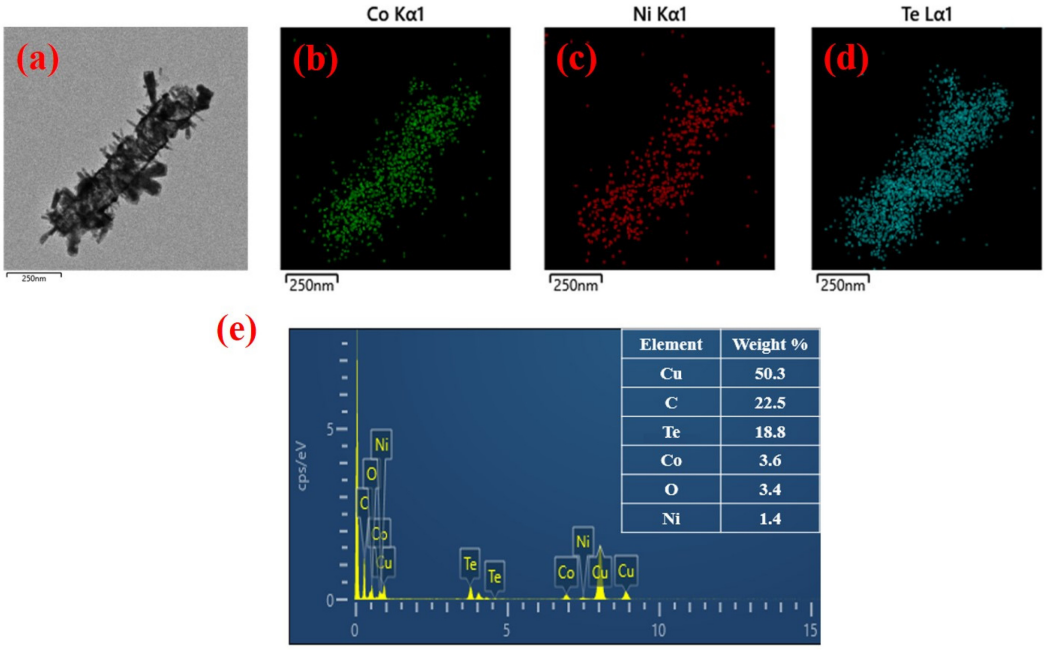

Figure 3. (**a**) STEM image of $CoNiTe_2$ nanomaterials and their corresponding element mapping images for (**b**) Co, (**c**) Ni, and (**d**) Te; (**e**) EDS spectrum of $CoNiTe_2$ nanomaterials.

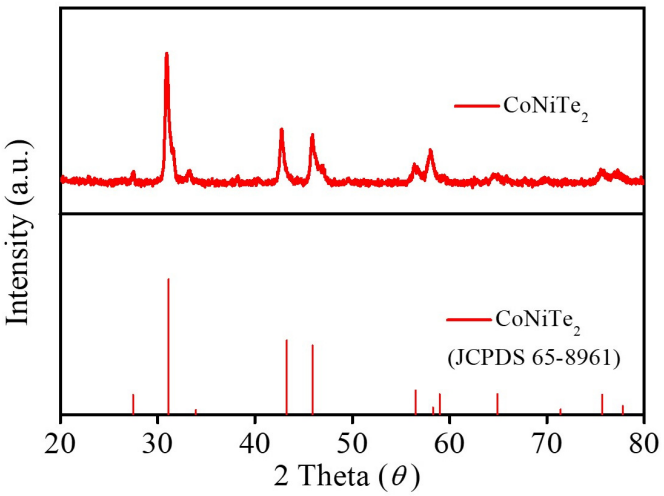

Figure 4. XRD patterns of $CoNiTe_2$ nanomaterials.

The surface elemental composition and valence states of the $CoNiTe_2$ nanomaterials were characterized by XPS, as shown in Figure 5. Figure 5a shows the high-resolution Co 2p XPS spectra of the $CoNiTe_2$ nanomaterials. Two spin-orbit doublets corresponding to Co $2p_{3/2}$ and Co $2p_{1/2}$ were found. Co^{2+} was observed at 780.8 eV and 797.2 eV (binding energies), while Co^{3+} was observed at 778.8 eV and 796 eV. In addition to the two spin-orbit doublets, shake-up satellites (marked as Sat.) were observed adjacent to each doublet, located at 785.4 eV and 802.6 eV, respectively. Figure 5b shows the high-resolution Ni 2p XPS spectra of the $CoNiTe_2$ nanomaterials. Two spin-orbit doublets were ascribed to Ni $2p_{3/2}$ and Ni $2p_{1/2}$. Ni^{3+} was located at binding energies 855.4 eV and 873.4 eV, while Ni^{2+} was observed at binding energies 852.4 eV and 870.2 eV. Likewise, two shake-up satellites (marked as Sat.) were observed adjacent to the two spin-orbit doublets, which were situated at 861.4 eV and 879.0 eV, respectively. Figure 5c shows the high-resolution Te 3d XPS spectra of the $CoNiTe_2$ nanomaterials. The spin-orbit doublets of Te $3d_{5/2}$ and Te $3d_{3/2}$ appeared at 573 eV and 583.4 eV, respectively, and are attributable to Te^{2-}. The other two peaks at 576 eV and 586.4 eV are shake-up satellites (marked as Sat.) [29].

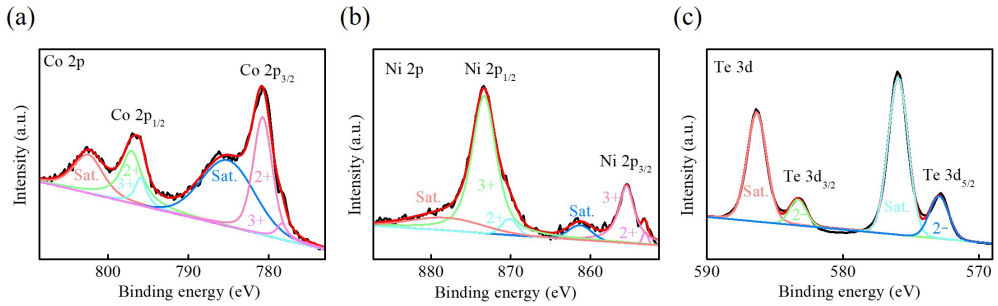

Figure 5. (**a**) Co 2p, (**b**) Ni 2p, and (**c**) Te 3d XPS spectra of $CoNiTe_2$ nanomaterials.

The electrochemical characteristics of $CoNiTe_2$ nanomaterials for DA detection were performed by cyclic voltammetry (CV). Figure 6 shows the CV curves of bare GCE (black lines), Nafion/GCE (blue lines), and $CoNiTe_2$/Nafion/GCE (red lines) in 0.1 M PBS (pH 7.0) in the absence (dashed lines) and presence (solid lines) of 1 mM DA at a 50 mV s^{-1} scan rate within the 0–1.0 V potential window. In the absence of DA, all electrodes show no redox peaks due to the absence of redox-active species. With the addition of 1 mM DA, all electrodes exhibited well-defined peaks (especially the $CoNiTe_2$/Nafion/GCE electrode) related to the electrochemical DA redox reaction mechanism. The possible electrochemical DA redox reaction mechanism is described in the previous literature [30]. During the electrochemical oxidation process, DA was oxidized to dopaminoquinone (DAQ), and during the electrochemical reduction process, DAQ was reduced to DA. The electrochemical DA redox reaction is a reversible process involving two electron/two proton transfers. Notably, $CoNiTe_2$/Nafion/GCE possesses the highest electrocatalytic activity in DA sensing. These results demonstrate that the synergistic interaction of bimetallic Co and Ni, the low electronegativity of Te, and the unique morphology of $CoNiTe_2$ nanorods improved electrochemical performance. According to a previous report [31], bimetallic Ni–Co transition metal chalcogenides generally exhibited satisfactory electrochemical performance. In Ni–Co tellurides, the electronegativity of Te is lower than those of S and Se. This results in weakened covalent bonding between the transition metal and Te, further accelerating electron transfer and modulating electronic structure in the electrochemical process. This enhanced electrochemical performance.

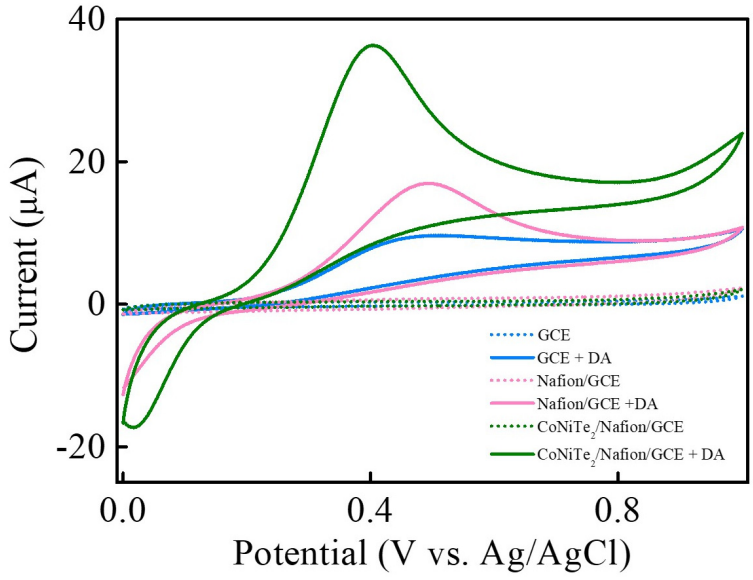

Figure 6. CV curves of bare GCE (blue line), Nafion/GCE (pink line), and $CoNiTe_2$/Nafion/GCE (green line) in 0.1 M PBS (pH 7.0) in the absence (dashed line) and presence (solid line) of 1 mM DA at a scan rate of 50 mV s^{-1}.

To obtain $CoNiTe_2$ nanomaterials with optimal electrochemical performance for DA sensing, the $CoNiTe_2$ loading amounts and pH values of the phosphate buffer solution were varied to understand electrochemical parameter optimization. To do this, 1~4 mg of $CoNiTe_2$ was weighed and dispersed into 1 mL 0.5 wt % Nafion to form a homogenous dispersion, then immobilized on the surface of GCE by a drop-casting method. Figure 7a shows the CV curves of $CoNiTe_2$/Nafion/GCE at different $CoNiTe_2$ loading amounts in 0.1 M PBS (pH 7.0) in the presence of 1 mM DA at a scan rate of 50 mV s^{-1}. It was observed that the oxidation peak current dramatically increased as the $CoNiTe_2$ loading amount varied from 1 to 2 mg. However, when the $CoNiTe_2$ loading amount exceeded 2 mg, the oxidation peak current decreased, indicating that the presence of the excess $CoNiTe_2$ hindered the mass transfer of dopamine [32]. Figure 7b displays the $CoNiTe_2$/Nafion/GCE CV curves at different phosphate buffer solution pH values (from pH 5 to 8) in the presence of 1 mM DA. The oxidation peak potential (E_{pa}) decreased with increasing pH value from 5 to 8, revealing that DA electrochemical behavior is associated with the pH dependence of interfacial electron–proton transfer. The corresponding linear relationship between oxidation peak potential and pH was calculated as follows: E_{pa} (V) = 0.846–0.059 pH (R^2 = 0.9771) (see the inset of Figure 7b). The results indicate a 0.059 V/pH linear slope. This is close to the theoretical value, implying that the electrochemical DA redox reaction mechanism involves two electron/two proton transfer steps, as governed by the Nernst equation [33]. Notably, the oxidation peak current increased slightly as the pH increased from 5 to 6, and then decreased rapidly from pH 6 to 8. The maximum DA oxidation peak current was at pH 6. Consequently, 2 mg of $CoNiTe_2$ (loading amount) and a phosphate buffer solution pH of 6.0 (pH value) were selected as the optimal parameters for DA sensing.

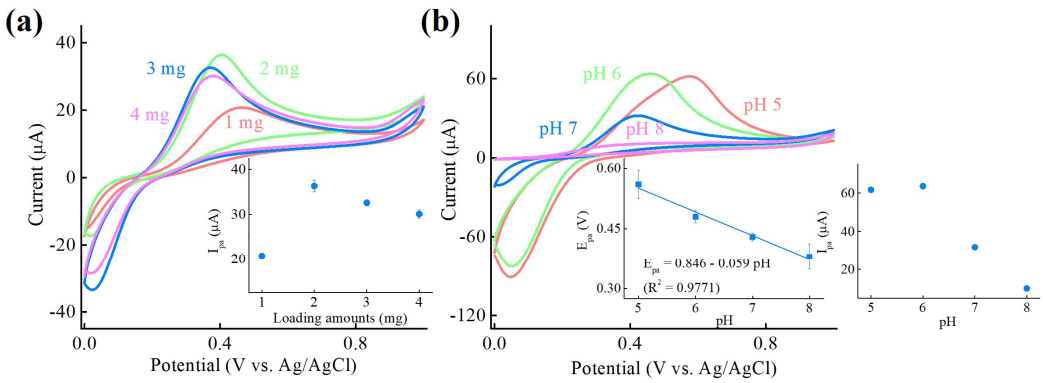

Figure 7. CV curves of $CoNiTe_2$/Nafion/GCE with different (**a**) $CoNiTe_2$ loading amounts (1~4 mg) and (**b**) pH values of phosphate buffer solution (pH 5.0~8.0) in 0.1 M PBS in the presence of 1 mM DA at a scan rate of 50 mV s^{-1}. Inset of (**a**): plot of the oxidation peak current (I_{pa}) vs. different $CoNiTe_2$ loading amounts. Bottom right inset of (**b**): plot of the oxidation peak current (I_{pa}) vs. pH. Bottom left inset of (**b**): plot of the oxidation peak potential (E_{pa}) vs. pH. (The error bars stand for the standard deviation of 3 repeat measurements).

To further examine the electrochemical behavior of the $CoNiTe_2$ nanomaterials, $CoNiTe_2$/Nafion/GCE was studied through CV performed in 0.1 M PBS (pH 6.0) in the presence of 1 mM DA at 50 to 300 mV s^{-1} scan rates (Figure 8a). It was observed that the redox peak current increased with increasing scan rate. Figure 8b reveals that both the oxidation peak current (I_{pa}) and reduction peak current (I_{pc}) were linear with the square root of the scan rate ($v^{1/2}$). The linear regression equation is expressed as I_{pa} (μA) = 34.8800 + 3.2760 $v^{1/2}$ ((mV s^{-1})$^{1/2}$) (R^2 = 0.9856) and I_{pc} (μA) = −22.7890–5.0160 $v^{1/2}$ ((mV s^{-1})$^{1/2}$) (R^2 = 0.9897). These results establish that the electrochemical DA redox reaction is controlled by diffusion according to the Randles–Sevcik equation [34].

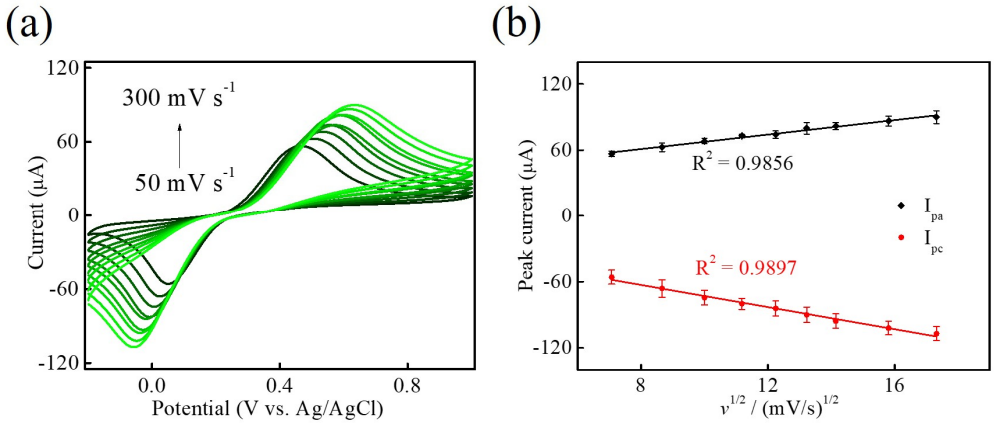

Figure 8. (**a**) CV curves of $CoNiTe_2$/Nafion/GCE in 0.1 M PBS (pH 6.0) in the presence of 1 mM DA at different scan rates from 50 mV s^{-1} to 300 mV s^{-1}. (**b**) The plot of the oxidation peak current (I_{pa}) and reduction peak current (I_{pc}) vs. square root of scan rate ($v^{1/2}$) (the error bars stand for the standard deviation of 3 repeat measurements).

We measured the electrochemical performance of $CoNiTe_2$/Nafion/GCE for DA electrooxidation using differential pulse voltammetry (DPV) in 0.1 M PBS (pH 6.0) with increasing DA concentrations (0~100 μM) under optimal experimental parameters to evaluate the feasibility of the proposed electrochemical non-enzymatic DA sensing. Figure 9a shows the $CoNiTe_2$/Nafion/GCE DPV responses against various DA concentrations from 0 to 100 μM. It was observed that the DPV response increased with increasing DA concentration. The DPV responses corresponding to DA concentrations ranging from 0.05 to 100 μM were plotted to obtain the corresponding calibration curve (Figure 9b). The linear regression equation for the oxidation peak current (I_{pa}) against the DA concentration is expressed as I_{pa} (μA) = 1.0030 + 0.0910 C (μM). The DA sensor calibration curve was linear from 0.05 to 100 μM (R^2 = 0.9928), and the slope and intercept were 0.0910 μA μM^{-1} and 1.0030 μA, respectively. The sensitivity (according to the geometric area of GCE (0.0707 cm^2) and the slope of the calibration curve), limit of detection (LOD) based on 3 S_b/m, and limit of quantification (LOQ) based on 10 S_b/m (S_b is the blank signal standard deviation for n = 3, and m is the calibration plot slope) were estimated as 1.2880 μA μM^{-1} cm^{-2}, 0.0380 μM, and 0.1270 mM, respectively. Table 1 summarizes previous reports regarding electrochemical non-enzymatic DA sensors based on the different transition metal chalcogenides [21,35–37]. It is noted that the $CoNiTe_2$ electrode material is comparable to the other electrochemical non-enzymatic DA sensors based on the different transition metal chalcogenides.

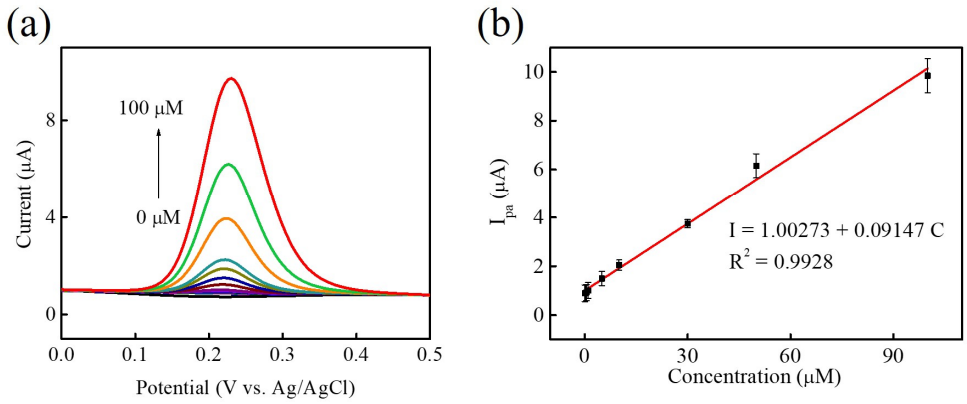

Figure 9. (**a**) DPV response of $CoNiTe_2$/Nafion/GCE in 0.1 M PBS (pH 6.0) with the successive addition of various DA concentrations from 0 to 100 μM. (**b**) The plot of DPV response vs. DA concentration.

Table 1. Comparison of electrochemical DA sensor performance based on the different transition metal chalcogenides.

Electrode Materials	Linear Range (mM)	Sensitivity ($\mu A\ \mu M^{-1}\ cm^{-2}$)	LOD (μM)	Reference
$NiCo_2S_4$/NF	0.50~100	14.9920	0.200	[35]
Sb_2S_3/GO/GCE	1.55~15.55	0.3077	0.800	[36]
fGO-$Ga_{0.7}Fe_{0.3}Se_2$/GCE	2~170	0.2188	0.110	[21]
Bi_2Te_3/rGO/GCE	10~1000	0.2229	0.060	[37]
$CoNiTe_2$/GCE	0.05~100	1.2880	0.038	This Work

In a physiological environment, the electrochemical similarities between dopamine (DA), uric acid (UA), and ascorbic acid (AA) biomolecules can cause overlapping detection signals, potentially impacting DA sensing accuracy and reliability. Therefore, it is necessary to perform an interference study to evaluate the sensing ability and distinguish the interfering species. This ensures the accurate determination of the target molecules. To evaluate the selectivity of the $CoNiTe_2$ nanomaterials in the presence of the interfering molecules for DA sensing, Figure 10 displays the interference effect results for $CoNiTe_2$/Nafion/GCE in 0.1 M PBS (pH 6.0) in the presence of 200 μM AA and 10 μM UA (both are reasonable concentrations in the human body) and various DA concentrations (0.05, 0.5, 1, 3, 5, 7.5, and 10 μM). As observed, the DPV responses of the interfering molecules AA and UA were found at 0.15 V and 0.35 V, respectively. However, the DPV response of DA was observed at about 0.22 V, and its response increased with increasing DA concentration. In the experimental results, no significant interference effect was observed for DA determination in the presence of AA and UA. The linear regression equation for the oxidation peak current (I_{pa}) against the DA concentration in the presence of AA and UA (interference effect) is expressed as I_{pa} (μA) = 2.3262 + 0.1401 C (μM). The calibration curve was linear from 0.05 to 10 μM (R^2 = 0.9946), and the slope and intercept were 0.1401 $\mu A\ \mu M^{-1}$ and 2.3262 μA, respectively. For interference effect evaluation, a comparison of slope differences in the solvent and interference addition calibration curves showed that there was a small increase in slope in the presence of interfering molecules, indicating a slight interference effect. To minimize interference effects, a quantitative analysis was further performed using matrix-matched calibration curves to reduce interference-induced effects. As discussed above, it can be deduced that $CoNiTe_2$/Nafion/GCE has acceptable selectivity at DA concentrations ranging from 0.05 to 10 μM when AA and UA were also present, demonstrating the excellent anti-interference ability of the $CoNiTe_2$ nanomaterials.

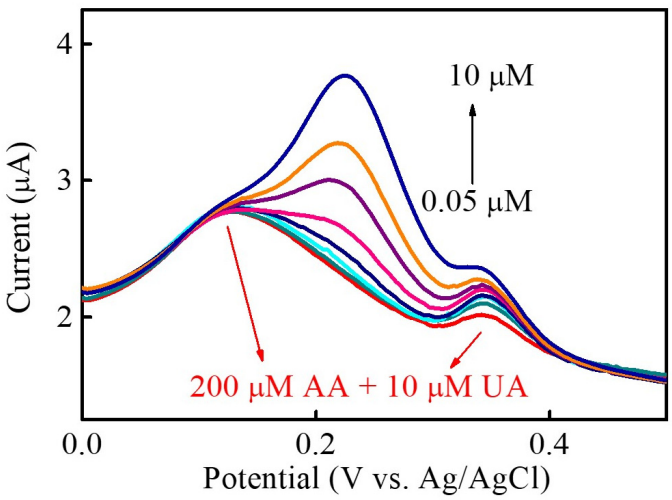

Figure 10. Interference study of $CoNiTe_2$/Nafion/GCE in 0.1 M PBS (pH 6.0) with the various DA concentration (0.05, 0.5, 1, 3, 5, 7.5, and 10 μM), as well as 200 μM AA and 10 μM UA.

4. Conclusions

In this study, a hydrothermally synthesized $CoNiTe_2$ nanomaterial-fabricated sensing platform ($CoNiTe_2$/Nafion/GCE) demonstrated prominent electrochemical performance for DA sensing owing to its excellent properties caused by bimetallic Co and Ni, the low electronegativity of Te, and its unique structural features (nanorods). In $CoNiTe_2$ nanomaterials, the lower electronegativity of Te leads to a weakened covalent bonding between transition metals and Te, resulting in the modulation of the electronic structure, which could propose an effective way to accelerate electron/ion transportation between the interface of the electroactive materials and electrolyte solution, exhibiting remarkable electrochemical performance for DA sensing. The electrochemical non-enzymatic DA sensor based on a $CoNiTe_2$ nanomaterials sensing platform exhibits excellent performance for the linear range from 0.05 to 100 μM, a sensitivity of 1.2880 μA μM^{-1} cm^{-2}, and a limit of detection (LOD) of 0.0380 μM. Furthermore, the acceptable selectivity of the presented $CoNiTe_2$/Nafion/GCE in the presence of interfering species makes it a promising DA sensing platform for it practical use.

Author Contributions: Conceptualization, H.-W.C. and Y.-C.T.; methodology, H.-W.C., Z.-Y.W., C.-H.S. and S.-H.Y.; software, Z.-Y.W., C.-H.S. and S.-H.Y.; formal analysis, H.-W.C., Z.-Y.W., C.-H.S. and S.-H.Y.; investigation, H.-W.C., Z.-Y.W., C.-H.S., S.-H.Y. and Y.-C.T.; data curation, H.-W.C., Z.-Y.W., C.-H.S. and S.-H.Y.; writing—original draft preparation, H.-W.C., Z.-Y.W. and Y.-C.T.; writing—review and editing, H.-W.C. and Y.-C.T.; visualization, H.-W.C.; supervision, H.-W.C. and Y.-C.T.; project administration, H.-W.C. and Y.-C.T. All authors have read and agreed to the published version of the manuscript.

Funding: This research was funded by the National Science and Technology Council (NSTC), Taichung Veterans General Hospital (TCVGH), and National United University (NUU), Taiwan (NSTC 112-2221-E-239-001-MY3, NSTC 112-2221-E-005-007-MY3, TCVGH-NUU1128901, TCVGH-NUU1138902, and SE113002).

Institutional Review Board Statement: Not applicable.

Informed Consent Statement: Not applicable.

Data Availability Statement: The data presented in this study are available on request from the corresponding author. The data are not publicly available due to privacy.

Acknowledgments: The authors are grateful to the NSTC and NUU for the financial assistance granted in support of this work. For instrumentation support, we thank the NSTC and the Instrument Center of National Chung Hsing University, Taiwan, for help with FESEM, HRTEM, and XPS measurements (NSTC 112-2740-M-005-001).

Conflicts of Interest: The authors declare no conflicts of interest.

References

1. Carlsson, A. Evidence for a role of dopamine in extrapyramidal functions. *Acta Neuroveg.* **1964**, *26*, 484–493. [CrossRef] [PubMed]
2. Thomas, R.; Pooventhiran, T.; Bakht, M.A.; Alzahrani, A.Y.; Salem, M.A. Study of interaction between different solvents and neurotransmitters dopamine, l-adrenaline, and l-noradrenaline using LED, QTAIM and AIMD. *J. Mol. Liq.* **2022**, *368*, 120708. [CrossRef]
3. Gaskill, P.J.; Khoshbouei, H. Dopamine and norepinephrine are embracing their immune side and so should we. *Curr. Opin. Neurobiol.* **2022**, *77*, 102626. [CrossRef] [PubMed]
4. Jo, Y.S.; Lee, J.; Mizumori, S.J. Effects of prefrontal cortical inactivation on neural activity in the ventral tegmental area. *J. Neurosci.* **2013**, *33*, 8159–8171. [CrossRef] [PubMed]
5. Douma, E.H.; de Kloet, E.R. Stress-induced plasticity and functioning of ventral tegmental dopamine neurons. *Neurosci. Biobehav. Rev.* **2020**, *108*, 48–77. [CrossRef] [PubMed]
6. Surmeier, D.J.; Guzman, J.N.; Sanchez-Padilla, J.; Schumacker, P.T. The role of calcium and mitochondrial oxidant stress in the loss of substantia nigra pars compacta dopaminergic neurons in Parkinson's disease. *Neuroscience* **2011**, *198*, 221–231. [CrossRef] [PubMed]
7. Wegrzynowicz, M.; Bar-On, D.; Calo', L.; Anichtchik, O.; Iovino, M.; Xia, J.; Ryazanov, S.; Leonov, A.; Giese, A.; Dalley, J.W. Depopulation of dense α-synuclein aggregates is associated with rescue of dopamine neuron dysfunction and death in a new Parkinson's disease model. *Acta Neuroveg.* **2019**, *138*, 575–595. [CrossRef] [PubMed]

8. Ayano, G. Dopamine: Receptors, functions, synthesis, pathways, locations and mental disorders: Review of literatures. *J. Ment. Disord. Treat.* **2016**, *2*, 2. [CrossRef]
9. Blum, T.; Moreno-Pérez, A.; Pyrski, M.; Bufe, B.; Arifovic, A.; Weissgerber, P.; Freichel, M.; Zufall, F.; Leinders-Zufall, T. Trpc5 deficiency causes hypoprolactinemia and altered function of oscillatory dopamine neurons in the arcuate nucleus. *Proc. Natl. Acad. Sci. USA* **2019**, *116*, 15236–15243. [CrossRef]
10. Zhuo, S.; Guan, Y.; Li, H.; Fang, J.; Zhang, P.; Du, J.; Zhu, C. Facile fabrication of fluorescent Fe-doped carbon quantum dots for dopamine sensing and bioimaging application. *Analyst* **2019**, *144*, 656–662. [CrossRef]
11. Liu, X.; He, F.; Zhang, F.; Zhang, Z.; Huang, Z.; Liu, J. Dopamine and melamine binding to gold nanoparticles dominates their aptamer-based label-free colorimetric sensing. *Anal. Chem.* **2020**, *92*, 9370–9378. [CrossRef]
12. Zhang, L.; Tang, Z.; Dong, Y. Silicon quantum dot involved luminol chemiluminescence and its sensitive detection of dopamine. *Anal. Methods* **2018**, *10*, 4129–4135. [CrossRef]
13. De Benedetto, G.E.; Fico, D.; Pennetta, A.; Malitesta, C.; Nicolardi, G.; Lofrumento, D.D.; De Nuccio, F.; La Pesa, V. A rapid and simple method for the determination of 3, 4-dihydroxyphenylacetic acid, norepinephrine, dopamine, and serotonin in mouse brain homogenate by HPLC with fluorimetric detection. *J. Pharm. Biomed. Anal.* **2014**, *98*, 266–270. [CrossRef] [PubMed]
14. Zhao, Y.; Zhao, S.; Huang, J.; Ye, F. Quantum dot-enhanced chemiluminescence detection for simultaneous determination of dopamine and epinephrine by capillary electrophoresis. *Talanta* **2011**, *85*, 2650–2654. [CrossRef] [PubMed]
15. Shahzad, F.; Iqbal, A.; Zaidi, S.A.; Hwang, S.-W.; Koo, C.M. Nafion-stabilized two-dimensional transition metal carbide ($Ti_3C_2T_x$ MXene) as a high-performance electrochemical sensor for neurotransmitter. *J. Ind. Eng. Chem.* **2019**, *79*, 338–344. [CrossRef]
16. Dong, Y.; Liu, J.; Zheng, J. A sensitive dopamine electrochemical sensor based on hollow zeolitic imidazolate framework. *Colloids Surf. A Physicochem. Eng. Asp.* **2021**, *608*, 125617. [CrossRef]
17. Xie, F.; Yang, M.; Jiang, M.; Huang, X.-J.; Liu, W.-Q.; Xie, P.-H. Carbon-based nanomaterials–a promising electrochemical sensor toward persistent toxic substance. *TrAC Trends Anal. Chem.* **2019**, *119*, 115624. [CrossRef]
18. Ahammad, A.S.; Akter, T.; Al Mamun, A.; Islam, T.; Hasan, M.M.; Mamun, M.; Faraezi, S.; Monira, F.; Saha, J.K. Cost-effective electrochemical sensor based on carbon nanotube modified-pencil electrode for the simultaneous determination of hydroquinone and catechol. *J. Electrochem. Soc.* **2018**, *165*, B390. [CrossRef]
19. Nair, J.A.; Saisree, S.; Aswathi, R.; Sandhya, K. Ultra-selective and real-time detection of dopamine using molybdenum disulphide decorated graphene-based electrochemical biosensor. *Sens. Actuators B Chem.* **2022**, *354*, 131254. [CrossRef]
20. Sakthivel, R.; Kubendhiran, S.; Chen, S.-M.; Kumar, J.V. Rational design and facile synthesis of binary metal sulfides VS_2-SnS_2 hybrid with functionalized multiwalled carbon nanotube for the selective detection of neurotransmitter dopamine. *Anal. Chim. Acta* **2019**, *1071*, 98–108. [CrossRef]
21. Baye, A.F.; Appiah-Ntiamoah, R.; Amalraj, J.; Reddy, K.K.; Kim, H. Graphene oxide interlayered Ga-doped $FeSe_2$ nanorod: A robust nanocomposite with ideal electronic structure for electrochemical dopamine detection. *Electrochim. Acta* **2020**, *363*, 137245. [CrossRef]
22. Padmanaban, A.; Padmanathan, N.; Dhanasekaran, T.; Manigandan, R.; Srinandhini, S.; Sivaprakash, P.; Arumugam, S.; Narayanan, V. Hexagonal phase Pt-doped cobalt telluride magnetic semiconductor nanoflakes for electrochemical sensing of dopamine. *J. Electroanal. Chem.* **2020**, *877*, 114658. [CrossRef]
23. Yadav, S.; Yashas, S.R.; Shivaraju, H.P. Transitional metal chalcogenide nanostructures for remediation and energy: A review. *Environ. Chem. Lett.* **2021**, *19*, 3683–3700. [CrossRef]
24. Zhou, J.; Liu, F.; Lin, J.; Huang, X.; Xia, J.; Zhang, B.; Zeng, Q.; Wang, H.; Zhu, C.; Niu, L. Large-area and high-quality 2D transition metal telluride. *Adv. Mater.* **2017**, *29*, 1603471. [CrossRef] [PubMed]
25. Zaw, N.Y.W.; Jo, S.; Park, J.; Kitchamsetti, N.; Jayababu, N.; Kim, D. Clay-assisted hierarchical growth of metal-telluride nanostructures as an anode material for hybrid supercapacitors. *Appl. Clay Sci.* **2022**, *225*, 106539. [CrossRef]
26. De Silva, U.; Masud, J.; Zhang, N.; Hong, Y.; Liyanage, W.P.; Zaeem, M.A.; Nath, M. Nickel telluride as a bifunctional electrocatalyst for efficient water splitting in alkaline medium. *J. Mater. Chem. A* **2018**, *6*, 7608–7622. [CrossRef]
27. Brea, C.; Hu, G. Shifting and breaking scaling relations at transition metal telluride edges for selective electrochemical CO_2 reduction. *J. Mater. Chem. A* **2022**, *10*, 10162–10170. [CrossRef]
28. Qian, G.; Mo, Y.; Yu, C.; Zhang, H.; Yu, T.; Luo, L.; Yin, S. Free-standing bimetallic $CoNiTe_2$ nanosheets as efficient catalysts with high stability at large current density for oxygen evolution reaction. *Renew. Energy* **2020**, *162*, 2190–2196. [CrossRef]
29. Yang, F.; Yang, M.; Zhang, J.; Guo, H.; Zhang, T.; Yang, W. High-efficiency hybrid supercapacitor based on three-dimensional interconnected nitrogen-rich caCTF-1@ pC-C_3N_4 network and $NiCoTe_2$. *J. Alloys Compd.* **2022**, *911*, 164782. [CrossRef]
30. Wang, L.; Wang, J.; Yan, L.; Ding, Y.; Wang, X.; Liu, X.; Li, L.; Ju, J.; Zhan, T. Prussian Blue Analogue-Derived Iron Sulfide–Cobalt Sulfide Nanoparticle-Decorated Hollow Nitrogen-Doped Carbon Nanocubes for the Selective Electrochemical Detection of Dopamine. *ACS Sustain. Chem. Eng.* **2022**, *10*, 17230–17240. [CrossRef]
31. Zhang, S.; Yang, D.; Zhang, M.; Liu, Y.; Xu, T.; Yang, J.; Yu, Z.-Z. Synthesis of novel bimetallic nickel cobalt telluride nanotubes on nickel foam for high-performance hybrid supercapacitors. *Inorg. Chem. Front.* **2020**, *7*, 477–486. [CrossRef]
32. Deng, Z.-P.; Sun, Y.; Wang, Y.-C.; Gao, J.-D. A NiFe alloy reduced on graphene oxide for electrochemical nonenzymatic glucose sensing. *Sensors* **2018**, *18*, 3972. [CrossRef] [PubMed]
33. Li, F.; Ni, B.; Zheng, Y.; Huang, Y.; Li, G. A simple and efficient voltammetric sensor for dopamine determination based on ZnO nanorods/electro-reduced graphene oxide composite. *Surf. Interfaces* **2021**, *26*, 101375. [CrossRef]

34. Sahoo, R.C.; Moolayadukkam, S.; Thomas, S.; Zaeem, M.A.; Matte, H.R. Solution processed Ni_2Co layered double hydroxides for high performance electrochemical sensors. *Appl. Surf. Sci.* **2021**, *541*, 148270. [CrossRef]
35. Dai, H.; Chen, D.; Li, Y.; Cao, P.; Wang, N.; Lin, M. Voltammetric sensing of dopamine based on a nanoneedle array consisting of $NiCo_2S_4$ hollow core-shells on a nickel foam. *Mikrochim. Acta* **2018**, *185*, 157. [CrossRef] [PubMed]
36. Gao, L.; Ma, J.; Zheng, J. Solvothermal synthesis of Sb_2S_3-graphene oxide nanocomposite for electrochemical detection of dopamine. *J. Electrochem. Soc.* **2020**, *167*, 107503. [CrossRef]
37. Shen, H.; Jang, B.; Park, J.; Mun, H.-J.; Cho, H.-B.; Choa, Y.-H. In situ synthesis of a Bi_2Te_3-nanosheet/reduced-graphene-oxide nanocomposite for non-enzymatic electrochemical dopamine sensing. *Nanomaterials* **2022**, *12*, 2009. [CrossRef]